Construction of dendritic Pt–Pd bimetallic nanotubular heterostructure for advanced oxygen reduction

Wang, Mingwei; Hu, Zhiyi; Lv, Jieheng; Yin, Zhiwen; Xu, Zhewei; Liu, Jingfeng; Feng, Shihao; Wang, Xiaoqian; He, Jiazhen; Luo, Sicheng; Zhao, Dafu; Li, Hang; Luo, Xuemin; Liu, Qi; Liu, Damin; Su, Bao Lian; Zhao, Dongyuan; Liu, Yong

Published in:
Interdisciplinary Materials

DOI:
10.1002/idm2.12212

Publication date:
2024

Document Version
Publisher's PDF, also known as Version of record

Received: 6 April 2024 | Revised: 28 May 2024 | Accepted: 27 June 2024

DOI: 10.1002/idm2.12212

SHORT COMMUNICATION

Interdisciplinary Materials — Open Access — WILEY

Construction of dendritic Pt–Pd bimetallic nanotubular heterostructure for advanced oxygen reduction

Mingwei Wang[1] | **Zhiyi Hu**[1] | **Jieheng Lv**[1] | **Zhiwen Yin**[1] | **Zhewei Xu**[1] | **Jingfeng Liu**[1] | **Shihao Feng**[1] | **Xiaoqian Wang**[1] | **Jiazhen He**[1] | **Sicheng Luo**[1] | **Dafu Zhao**[1] | **Hang Li**[1] | **Xuemin Luo**[1] | **Qi Liu**[1] | **Damin Liu**[1] | **Baolian Su**[1,2] | **Dongyuan Zhao**[3] | **Yong Liu**[1]

[1]International School of Materials Science and Engineering (ISMSE), State Key Laboratory of Advanced Technology for Materials Synthesis and Processing, Wuhan University of Technology, Wuhan, China

[2]Department of Chemistry, Laboratory of Inorganic Materials Chemistry, University of Namur, Namur, Belgium

[3]Department of Chemistry, Laboratory of Advanced Materials, Shanghai Key Lab of Molecular Catalysis and Innovative Materials, State Key Laboratory of Molecular Engineering of Polymers, Fudan University, Shanghai, China

Correspondence
Yong Liu, International School of Materials Science and Engineering (ISMSE), State Key Laboratory of Advanced Technology for Materials Synthesis and Processing, Wuhan University of Technology, Wuhan 430070, China.
Email: liuyong3873@whut.edu.cn

Funding information
National Natural Science Foundation of China, Grant/Award Number: 52072281; Major Program of the National Natural Science Foundation of China, Grant/Award Number: 22293021; State Key Laboratory of Advanced Technology for Materials Synthesis and Processing, Wuhan University of Technology

Abstract

Compositions and morphologies of Pt-based electrocatalysts have great impact on the electrocatalytic activity and stability of oxygen reduction reaction (ORR). Herein, we report a novel design of one-dimensional (1D) Pt–Pd dendritic nanotubular heterostructures (DTHs) by controlling the degree of Pt^{2+}-Pt reduction reaction and Pd-Pt galvanic replacement reaction with uniform Pd nanowires as sacrificial templates. The obtained Pt–Pd bimetallic DTHs catalyst exhibited uniform and dense Pt dendritic nanobranches on the surface of 1D hollow Pt–Pd alloy nanotubes, possessing superior catalytic activity for ORR compared to state-of-the-art commercial Pt/C catalysts. Typically, the Pt_4Pd DTHs catalyst showed efficient mass activity (MA, 1.05 A mg_{Pt}^{-1}) and specific activity (SA, 1.25 mA cm_{Pt}^{-2}) at 0.9 V (vs. RHE), and the catalyst exhibited high stability with 90.4% MA retention after 20 000 potential cycles. The Pt–Pd bimetallic DTHs configuration combines the advantages of 1D hollow nanostructures and dense Pt dendritic nanobranches, which results in rich electrochemical active surface sites, fast charge transport, and multiple dendritic anchoring points contact on carbon support, thus boosting its catalytic activity and stability towards electrocatalysis.

KEYWORDS
dendritic hollow heterostructures, electrocatalysis, one-dimensional nanowires, oxygen reduction, proton exchange membrane fuel cells

Mingwei Wang, Zhiyi Hu, Jieheng Lv, and Zhiwen Yin contributed equally to this work.

1 | INTRODUCTION

Proton exchange membrane fuel cells (PEMFCs) have attracted a great deal of attention and are considered promising electrochemical energy conversion devices due to their high efficiency over Carnot cycle and without any pollution emissions. The oxygen reduction reaction (ORR) in PEMFCs exhibits sluggish kinetics and requires highly efficient electrocatalysis. Although platinum (Pt) nanoparticles supported on carbon black (Pt/C) are commercially the most efficient electrocatalysts, the Ostwald ripening process during the electrochemical cycle results in irreversible structural agglomeration and severe degradation of electrocatalyst activity.[1–3] In addition, the resource scarcity and high cost of Pt also hamper wide application of PEMFCs. To date, extensive efforts have been devoted to improving the performance of ORR catalysts. Alloying Pt with non-noble transition metal (M = Ni, Fe, Co, etc.) was considered an effective strategy for enhancing the catalytic activity and significantly increasing the utilization efficiency of Pt by precisely optimizing the composition and morphology. Alloying Pt with other metals can effectively reduce the unit area loading of Pt; unfortunately, the stability problem of Pt-based catalysts has not yet been solved or even more serious.[4,5] Hence, it is of great importance to design excellent Pt-based nanostructures that endow high activity, efficient Pt utilization, and long-term stability, which is highly desirable for applications in fuel cell catalysis reactions.

The geometric structural engineering of catalysts is an effective strategy for boosting electrocatalytic reactions. Considering the superior properties of one-dimensional (1D) nanostructure, such as inherent anisotropic merits, high surface area, fast charge transfer, superior flexibility, and good resistibility to dissolution, 1D Pt-based alloy nanostructures, including nanowires, nanofibers, nanorods, and nanotubes, are expected to be ideal structure for improving both the electrocatalytic activity and stability.[6,7] In particular, 1D dendritic nanotubular heterostructures (DTHs), which ideally integrate 1D hollow nanotubes with nano-sized dendrites, have attracted significant attention due to their unique structural advantages. Specifically, DTHs can maximize the active sites and offer fast transport paths for ions and electrons to boost the electrocatalytic activity. The aggregation and Ostwald ripening can be efficiently alleviated, and nano-sized dendrites endow multiple anchoring points to contact the carbon support for ORR in DTHs, leading to enhanced stability.[8–10] However, the rational design and construction of DTHs with controllable compositions and well-defined morphologies are still challenging.

Herein, we chose 1D Pd NWs as starting sacrificial template to successfully design highly efficient Pt–Pd bimetallic DTHs electrocatalysts. Interestingly, by controlling the degree of the reaction of L-ascorbic acid (AA) with $[PtCl_4]^{2-}$ to form dendritic Pt nanobranches on the surface of Pd NWs and the galvanic replacement reaction of Pd with $[PtCl_4]^{2-}$ to yield a hollow structure,[11,12] we prepared three different 1D Pt–Pd heterostructures: Pt_4Pd DTHs with dendritic dense Pt nanobranches, Pt_3Pd DTHs with dendritic short Pt nanobranches and Pt_2Pd dendritic solid nanowire heterostructures (Pt_2Pd DSHs). The Pt_4Pd DTHs/C showed the highest mass activity (MA) of 1.05 A mg_{Pt}^{-1} and a specific activity (SA) of 1.25 mA cm_{Pt}^{-2} at 0.9 V versus reversible hydrogen electrode (vs. RHE), which is 4.8 and 4.3 times higher than that of commercial Pt/C (0.22 A mg_{Pt}^{-1} and 0.29 mA cm_{Pt}^{-2}, respectively). Impressively, the Pt_4Pd DTHs exhibited superior electrocatalyst stability, with only a 5.1 mV shift in ORR polarization curves (maintaining 90.4% MA) over 20 000 potential cycles.

2 | RESULTS AND DISCUSSION

The synthesis of Pt–Pd bimetallic hollow DTHs and solid DSHs with different configurations is illustrated in Figure 1. First, single-crystalline Pd nanowires (NWs) were prepared through a hydrothermal reduction of sodium tetrachloropalladate (Na_2PdCl_4) with sodium iodide (NaI) and polyvinylpyrrolidone (PVP) in an aqueous solution (see details in Section 4).[13] Then, the Pt_2Pd DSHs, Pt_3Pd DTHs, and Pt_4Pd DTHs were successfully synthesized by using the as-synthesized Pd NWs as starting templates and AA as reducing agent. In the absence of AA, Pt_3Pd DTHs were obtained by Pd-Pt galvanic replacement reaction ($PtCl_4^{2-} + Pd \rightarrow Pt + PdCl_4^{2-}$) for 32 h due to the higher reduction potential of $[PtCl_4]^{2-}$/Pt (0.74 V vs. the RHE) than $[PdCl_4]^{2-}$/Pd (0.62 V vs. the RHE).[14,15] When 10 mM AA was regarded as the reductant, Pt_4Pd DTHs were obtained by competing Pt^{2+}-Pt reduction reaction ($C_6H_8O_6 + Pt^{2+} \rightarrow Pt + C_6H_6O_6 + 2H^+$) with Pd-Pt galvanic replacement reaction.[16,17] However, when excess AA (60 mM) was added to the reaction mixture, all $[PtCl_4]^{2-}$ ions were preferentially reduced by AA, and no extra $[PtCl_4]^{2-}$ ions were involved in galvanic replacement reaction, producing 1D Pt_2Pd bimetallic dendritic solid nanowire heterostructures (Pt_2Pd DSHs).[18,19]

The transmission electron microscopy (TEM) images showed that the starting Pd were nearly 100% in nanowire (NW) shape with uniform diameter of 9.4 ± 0.5 nm (Supporting Information SI: Figure S1). Aberration-correction high-resolution scanning tansmission electron

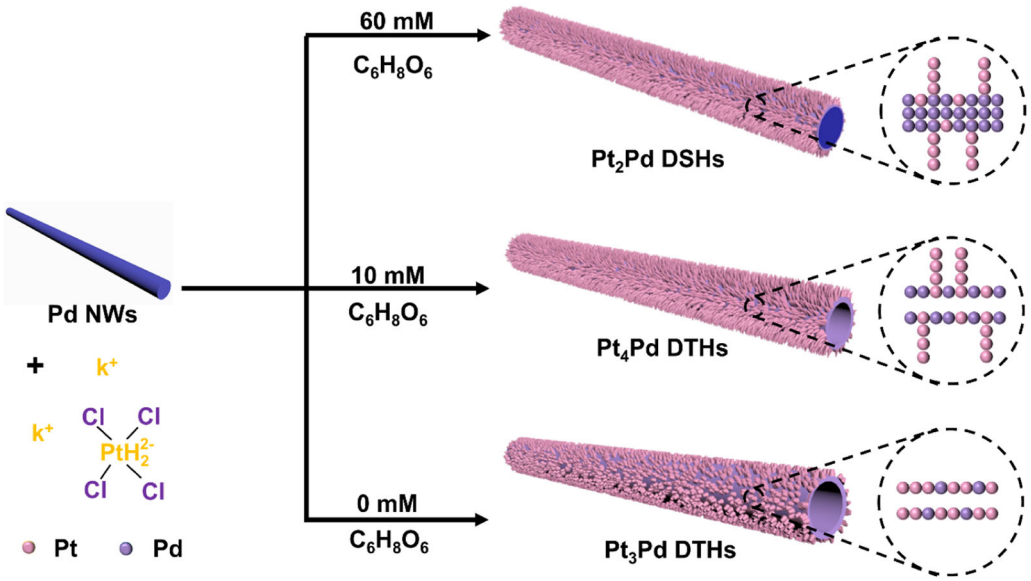

FIGURE 1 Schematic illustration of the synthesis of Pt_2Pd DSHs, Pt_4Pd DTHs and Pt_3Pd DTHs. DSHs, dendritic solid nanowire heterostructures; DTHs dendritic nanotubular heterostructures.

microscopy (AC-HRSTEM) further revealed that the Pd NWs had typical face centered-cubic (fcc) Pd (111) lattice spacing of 0.228 nm (Supporting Information: Figure S1f), indicating that Pd NWs are enclosed by (111) facets along its whole length.[20–22] AC-HRSTEM images also confirmed that the Pd NWs have a rough (111) surface with a high density of surface atomic steps/defects, which can provide rich active sites for subsequent Pt nucleation and/or galvanic replacement (Supporting Information: Figure S1e,f).[23–25] These defective Pd NWs were then used as sacrificial templates for the formation of Pt–Pd DTHs. Compared with the starting Pd NWs in Figure 2A, the TEM images in Figure 2B–D showed that the as-synthesized Pt_2Pd DSHs, Pt_4Pd DTHs, and Pt_3Pd DTHs had a much rougher surface with average diameters of 25.1, 25.5, and 18.1 nm, respectively. The average lengths of the dendritic branches of the Pt_2Pd DSHs and Pt_4Pd DTHs were calculated to be 7.85 and 8.05 nm, respectively. From the low-magnification TEM images, it was found that DSHs and DTHs nanostructures were the dominant products, with yields approaching near 100% after AA reduction and/or galvanic replacement reaction (Supporting Information: Figure S2).

To reveal the detailed structural characteristics and the element distribution of the Pt-Pt DTHs sample, high-angle annular dark-field scanning transmission electron microscopy (HAADF-STEM) and the corresponding energy-dispersive X-ray spectroscopy (EDS) mapping/line-scanning profiles were carried out (Figure 2). After only AA reduction reaction, the EDS mapping and line-scanning profile revealed that the resultant Pt_2Pd DSHs were solid dendritic nanostructure consisting of a core rich in Pd and a number of nanoarms rich in Pt (Figure 2B,F,J,N), confirming the presence of a dendritic solid nanowire heterostructure. However, after AA reduction reaction combined with galvanic replacement reaction, the resultant Pt_4Pd DTHs (Figure 2C,G,K,O) and Pt_3Pd DTHs (Figure 2D,H,L,P) both exhibited strongly enriched Pt/Pd atoms at the edge, and Pt was mainly distributed on the surface of the Pt–Pd bimetallic nanowires in the form of dendritic branches, confirming their dendritic Pt–Pd bimetallic hollow nanowire heterostructure. The elemental mapping of a single Pt_4Pd DTHs, Pt_3Pd DTHs, and Pt_2Pd DSHs reveals the dendrites on the outer wall of the nanotube are composed of Pt atoms, the inner wall of the nanotube is composed of Pd atoms, and the interface is Pt–Pd alloy phase, indicating that the formation of the heterostructure. (Supporting Information: Figure S4). The molar ratios of Pt to Pd on the Pt_2Pd DSHs, Pt_3Pd DTHs, and Pt_4Pd DTHs were calculated to be 67.8:32.2 (~2:1), 74.2:25.8 (~3:1), and 79.8:20.2 (~4:1) by TEM-EDS, respectively, which are consistent with the inductively coupled plasma optical emission spectrometer (ICP–OES) results (Supporting Information: Figure S3 and Table S1).

We further characterized crystalline nature and surface feature of Pt–Pd bimetallic DTHs samples by AC-HRSTEM. The AC-HRSTEM images showed that the exteriors of all DTHs samples are well covered by Pt dendrites with an average diameter of 2 nm (Figure 3 and Supporting Information: Figure S5). The Pt dendrites are highly branched in various directions, resulting in the porous wall in each individual DTHs entity. Figure 3C,F showed the Pt dendrites exhibit high

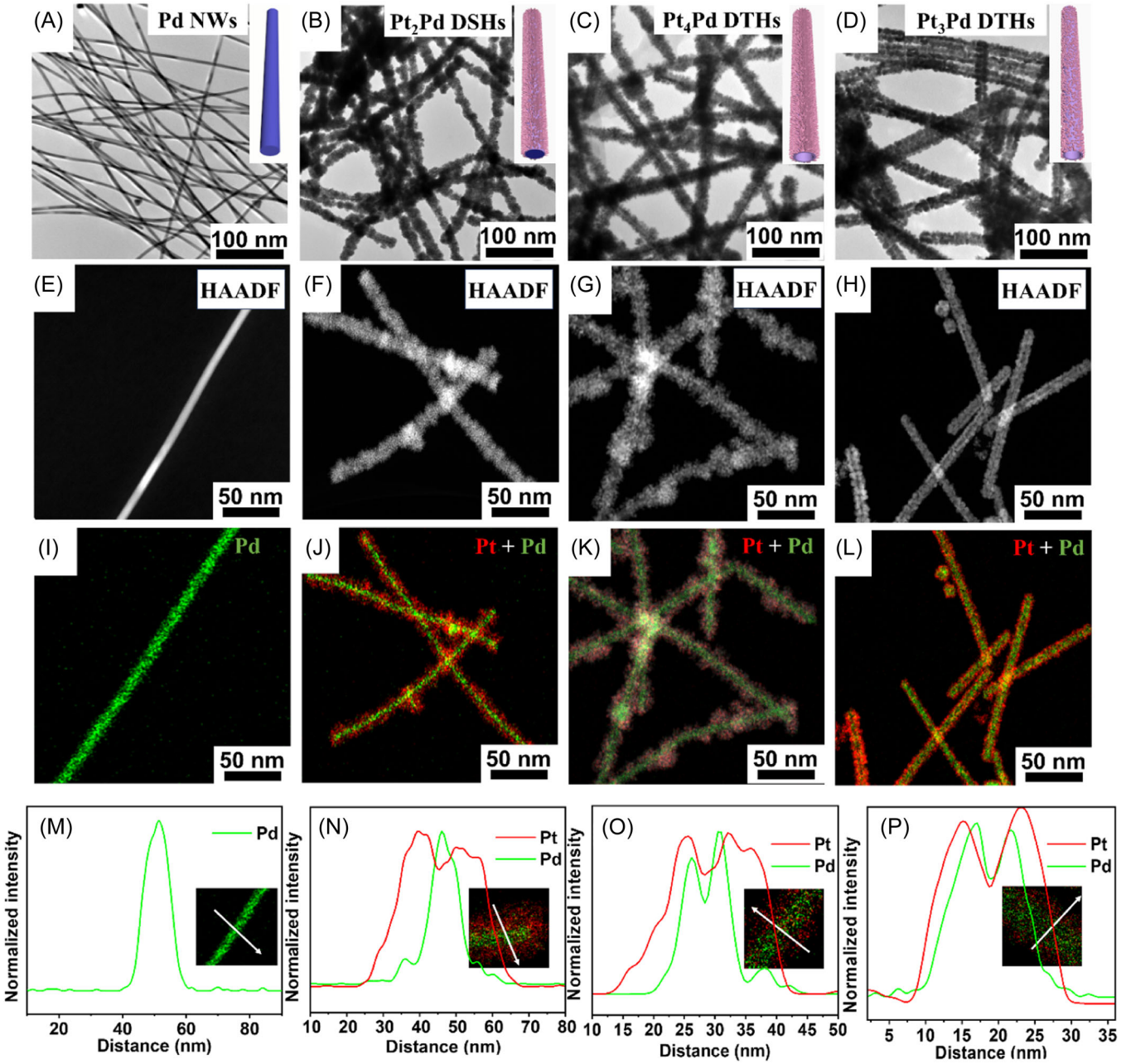

FIGURE 2 Structural and compositional characterization of Pd NWs, Pt_2Pd DSHs, Pt_3Pd DTHs, and Pt_4Pd DTHs. TEM images, high-angle annular dark-field scanning transmission electron microscopy (HAADF-STEM) images, the energy-dispersive X-ray spectroscopy (EDS) elemental mapping and the corresponding line-scanning profile of Pd NWs (A, E, I, and M), Pt_2Pd DSHs (B, F, J, and N), Pt_4Pd DTHs (C, G, K, and O), and Pt_3Pd DTHs (D, H, L, and P). DSHs, dendritic solid nanowire heterostructures; DTHs dendritic nanotubular heterostructures; NWs, nanowires.

crystallinity with well-resolved lattice spacing of 0.23 nm, corresponding to the (111) lattice plane of fcc Pt.[26–28] Impressively, the resultant dendritic Pt_3Pd and Pt_4Pd DTHs had well-developed hollow tubular interiors, which quite differed from the starting Pd NWs sample with solid interiors (Figure 3B–G). The Pt dendrites exhibit the lattice spacing of 0.23 nm, corresponding to the Pt (111) and the lattice fringe of 0.228 nm and 0.195 nm, corresponding to the Pd (111) and (200) (Figure 3D,G and Supporting Information: Figure S6). The HRSTEM images of the hollow tubular walls for Pt_3Pd and Pt_4Pd DTHs have (111) lattice spacings of 0.22 and 0.21 nm, respectively, which are slightly smaller than that of the (111) lattice plane of Pt (0.23 nm). The powder X-ray diffraction (XRD) patterns of the Pt_2Pd DSHs, Pt_4Pd DTHs, and Pt_3Pd DTHs also

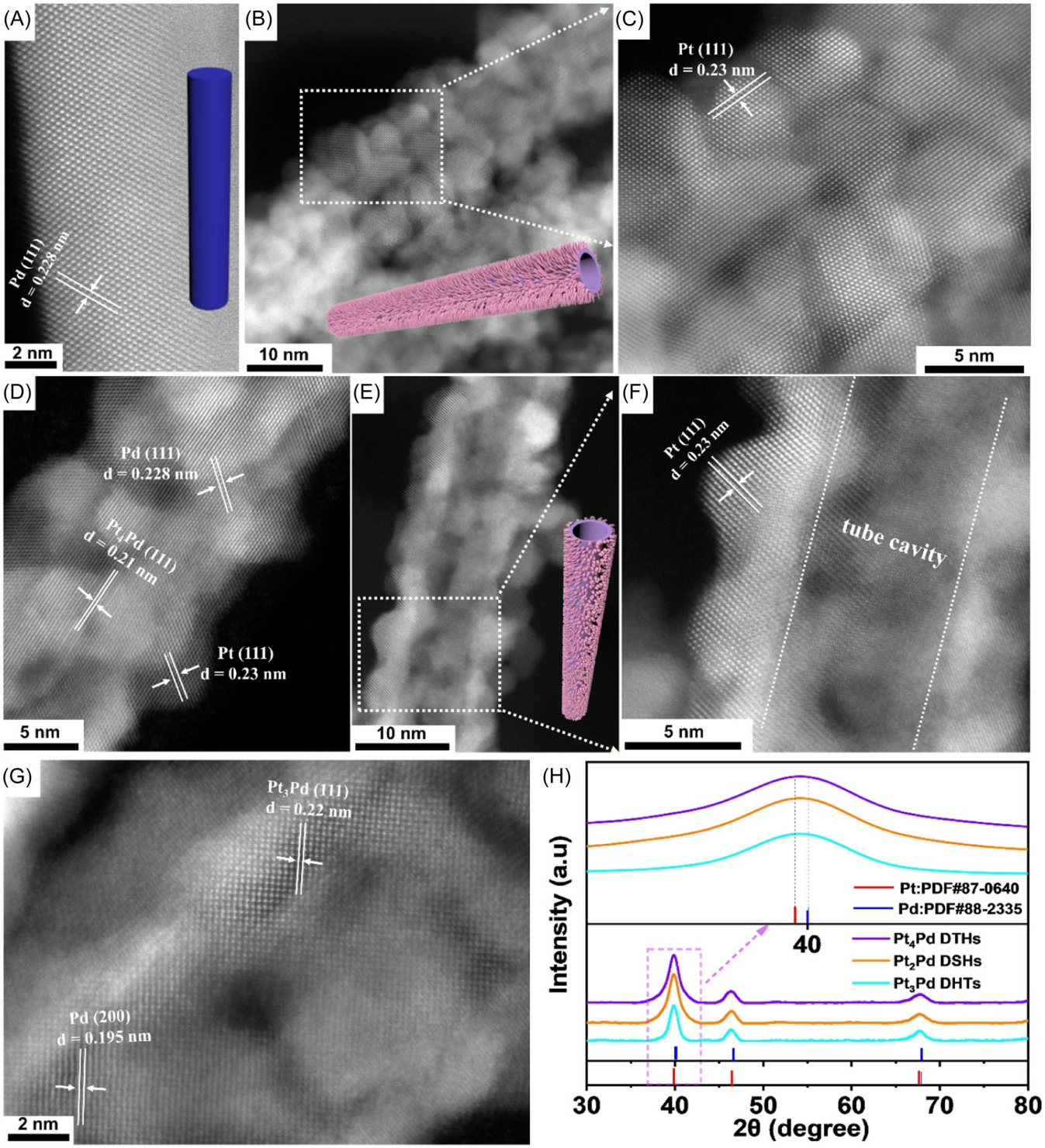

FIGURE 3 AC-HRSTEM images of (A) Pd NWs, (B–D) Pt_4Pd DTHs, (E–G) Pt_3Pd DTHs. (H) X-ray diffraction (XRD) patterns of Pt_2Pd DSHs, Pt_3Pd DTHs, and Pt_4Pd DTHs. AC-HRSTEM, aberration-correction high-resolution scanning transmission electron microscopy; DSHs, dendritic solid nanowire heterostructures; DTHs dendritic nanotubular heterostructures; NWs, nanowires.

showed an fcc structure (Figure 3H), with diffraction peaks slightly shifted to higher angle value compared to Pt, which could be attributed to the decrease in lattice distance when smaller Pd atoms were alloyed with Pt atoms in the lattice.[29–31]

The surface chemical states and electronic structures of the Pt_2Pd DSHs, Pt_4Pd DTHs and Pt_3Pd DTHs were further investigated by X-ray photoelectron spectroscopy (XPS). The survey spectrum demonstrated the presence of only Pt and Pd elements in the as-synthesized DTHs

samples (Supporting Information: Figure S7a–c). The high-resolution Pt 4f and Pd 3d spectra can be fitted into two spin-orbit doublets and two shake-up satellites (Supporting Information: Figure S7d–i). Compared with standard bulk Pt, the Pt 4f peaks for all Pt–Pd bimetallic DTHs samples shifted to a lower binding energies, whereas the peak of Pd 3d displayed a positive shift in comparison with the standard bulk Pd. The above remarkable shift of the binding energies for Pt 4f and Pd 3d in Pt–Pd bimetallic DTHs samples demonstrated that electrons were transferred from Pd to Pt. The above electron transfer synergistic effect of the Pt–Pd alloy may downshift the Pt d-band center, weaken the bonding strength between Pt and oxygen species, which can significantly optimize the catalytic performance of the Pt–Pd bimetallic DTHs for electrochemical reactions.[32–34]

To better understand the structural evolution from the starting Pd NWs to Pt–Pd bimetallic DTHs, the morphology/composition of the intermediate Pt_4Pd DTHs were taken out from the solution as a function of reaction time and analyzed by TEM and STEM-EDS. The TEM images showed different stages of the Pt^{2+}-Pt reduction/Pd-Pt galvanic replacement reaction between Pd NWs and K_2PtCl_4 (Supporting Information: Figure S8). Only well-defined Pd NWs existed in the reaction solution when the reaction time was less than 2 min (Supporting Information: Figure S8b,h). When the reaction time reached 3 min, Pt nanobranches (~4 nm) began to appear on the surface of Pd NWs by means of the deposition and epitaxial growth of Pt atoms, which were reduced by AA (Supporting Information: Figure S8c). When the reaction time was extended to 2 h, the density and length of the Pt nanobranches (~6 nm) increased, and some parts of Pd NWs started to form hollow voids (Supporting Information: Figure S8d). The above results indicated that AA was completely consumed, and the residual $[PtCl_4]^{2-}$ immediately started a galvanic replacement reaction with Pd NWs (Supporting Information: Figure S8d,i). Figure S8e–g,j showed the galvanic replacement reaction was completed when the reaction proceeded to 32 h, and Pt dendrites became denser, and the length increased to approximately 8 nm, eventually leading to the formation of high-quality dendritic Pt–Pd tubular heterostructures (Pt_4Pd DTHs). The diameter changes of the Pt_4Pd DTHs at different reaction times are shown in Supporting Information: Figure S9. Based on the above observations at different periods, the possible growth mechanism of Pt_4Pd DTHs could be inferred as follows (schematic illustration of the formation of Pt_4Pd DTHs in Supporting Information: Figure S8a). First, the Pt atoms were preferentially reduced and selectively deposited on the surface of Pd NWs by reduction reaction between Pt^{2+} and AA due to the high rate of Pt reduction. Meanwhile, once Pt nucleates on the surface of Pd NWs, the Pt nuclei can serve as catalytic sites for further reduction of $[PtCl_4]^{2-}$, and deposition preferentially occurs on the Pt nuclei to form well-defined Pt nanobranches.[12,35] After exhaustion of AA, the remaining $[PtCl_4]^{2-}$ and Pd atoms underwent a galvanic replacement reaction ($PtCl_4^{2-} + Pd \rightarrow Pt + PdCl_4^{2-}$), resulting in the continuous dissolution of Pd atoms from Pd NWs, leaving behind hollow voids in the Pd NWs as galvanic replacement reaction proceeded.[36–38] Finally, high-quality dendritic Pt–Pd nanotubular heterostructures were obtained as a result of completer consumption of $[PtCl_4]^{2-}$ and sacrificing Pd NWs after 32 h. In addition, the selection of Pd as the starting material for the sacrificial template because of its suitability for the galvanic replacement reaction to form hollow nanotubes, its ability to provide a rough surface for Pt nucleation, and the potential to create various heterostructures by controlling the reaction conditions.

The electrocatalytic properties of Pt_2Pd DSHs, Pt_3Pd DTHs, and Pt_4Pd DTHs catalysts for ORR was evaluated and benchmarked against the commercial Pt/C (20 wt % Pt on a Vulcan XC-72 carbon support, Pt particle size of 2–5 nm), and the results are compared in Figure 4 and Supporting Information: Figure S10–15. All the catalysts were dispersed in a mixture of ethanol/Nafion and homogeneously deposited on a glassy carbon electrode before electrochemical measurements. The cyclic voltammetry (CV) curves of all catalysts (tested in N_2-saturated 0.1 M $HClO_4$ solution at scan rates of 50 mV s^{-1}) showed two distinctive potential regions associated with the underpotentially deposited hydrogen (H_{upd}, $H^+ + e^- = H_{upd}$, $0 < E < 0.37$ eV) and absorbed hydroxyl species (OH_{ad}, $2H_2O = OH_{ad} + H_3O^+ + e^-$, $E > 0.7$ eV) (Figure 4A). The electrochemically active surface area (ECSA) calculated by the H_{upd} of the Pt_4Pd DTHs/C catalyst was 90.1 $m^2\ g_{Pt}^{-1}$, which is substantially higher than that of Pt_2Pd DSHs/C (83.8 $m^2\ g_{Pt}^{-1}$), Pt_3Pd DTHs/C (39.4 $m^2\ g_{Pt}^{-1}$) and the commercial Pt/C (70.5 $m^2\ g_{Pt}^{-1}$) catalysts. The above ECSA results demonstrated that the dense and long dendritic Pt nanobranches as well as hollow tubular nanostructures of the Pt_4Pd DTHs catalyst endowed more available exposed activated catalytic sites for electrocatalytic reaction.

Figure 4B showed the ORR polarization curves of the samples tested in O_2-saturated 0.1 M $HClO_4$ aqueous solution using a glass carbon rotating disk electrode (RDE) at room temperature. The half-wave potential ($E_{1/2}$) of the Pt_4Pd DTHs ($E_{1/2} = 0.891$ V), Pt_2Pd DSHs ($E_{1/2} = 0.871$ V), and Pt_3Pd DTHs ($E_{1/2} = 0.886$ V) showed a significant positive shift compared with commercial Pt/C ($E_{1/2} = 0.851$ V), demonstrating the enhanced ORR catalyst activities for the Pt–Pd bimetallic DTHs catalyst.

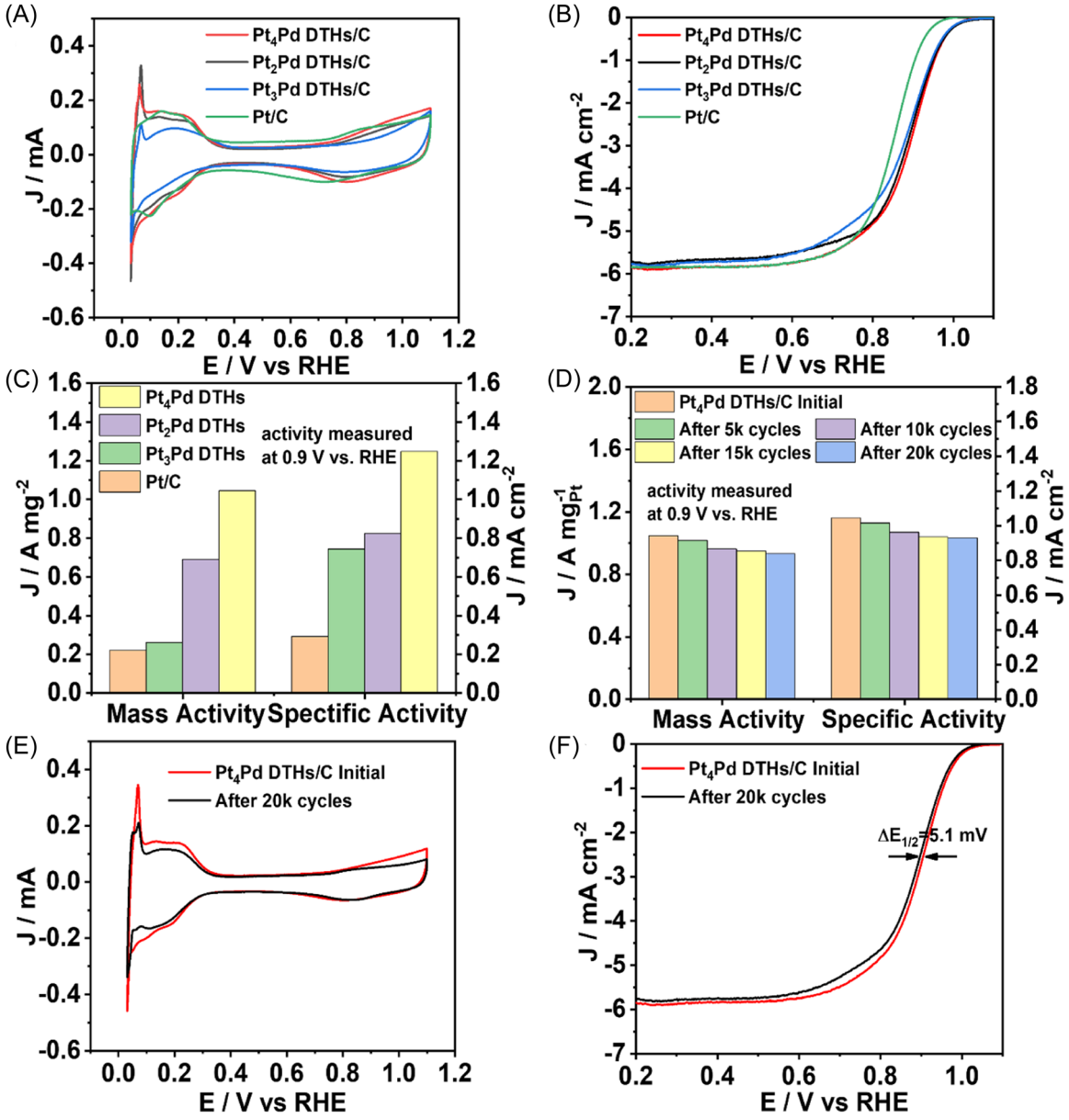

FIGURE 4 Electrocatalytic performance of Pt_4Pd DTHs/C, Pt_2Pd DSHs/C, Pt_3Pd DTHs/C and commercial Pt/C catalysts for ORR. (A) CV curves. (B) ORR polarization curves. (C) Mass and specific activities. (D) Mass and specific activity evolutions for Pt_4Pd DTHs/C before and after different potential cycles. (E) CV curve evolutions for Pt_4Pd DTHs/C before and after 20 000 potential cycles. (F) ORR polarization curve evolutions for Pt_4Pd DTHs/C before and after 20 000 potential cycles. CV, cyclic voltammetry; DSHs, dendritic solid nanowire heterostructures; DTHs dendritic nanotubular heterostructures; ORR, oxygen reduction reaction.

Subsequent Koutecky–Levich (K-L) plots of various catalysts originating from polarization curves at different rotation rates present a linear relationship between J^{-1} and $\omega^{-1/2}$. The number of transferred electrons calculated from the K-L equation was approximately 4.07, 4.02, 4.03, and 4.13 for commercial Pt/C, Pt_4Pd DTHs/C, Pt_2Pd DTHs/C, and Pt_3Pd DSHs/C, respectively, which suggested an efficient 4-electron reaction process for the above four catalysts (Supporting Information: Figure S14, S15). The specific activities (SA) of Pt_4Pd DTHs/C, Pt_2Pd DSHs/C, Pt_3Pd DTHs/C and commercial Pt/C were 1.25 mA cm_{Pt}^{-2}, 0.82 mA cm_{Pt}^{-2}, 0.74 mA cm_{Pt}^{-2}, and 0.31 mA cm_{Pt}^{-2} at 0.9 V versus RHE respectively. The mass activities (MA) of Pt_4Pd DTHs/C, Pt_2Pd DSHs/C, Pt_3Pd DTHs/C, and commercial Pt/C were 1.05 A mg_{Pt}^{-1}, 0.69 A mg_{Pt}^{-1}, 0.26 A mg_{Pt}^{-1}, and 0.22 A mg_{Pt}^{-1} at 0.9 V versus RHE (Figure 4C and Supporting Information: S10–S13), respectively. The above RDE test clearly confirmed that the ORR activity of the Pt_4Pd DTHs sample was much higher than that of the state-of-the-art commercial Pt/C catalyst, indicating that the 1D Pt–Pd bimetallic DTHs

catalyst were among the most active electrocatalysts for ORR reported to date.

The electrocatalytic durability of all the catalysts was tested by applying potential sweeps between 0.2 and 1.1 V versus RHE in 0.1 M $HClO_4$ solution at 50 mV s^{-1}. The CV and ORR polarization curve evolutions of Pt_4Pd DTHs/C before and after potential cycling in Figure 4E,F showed that the half-wave potential decreased by 5.1 mV after 20 000 potential cycles. The SA and MA of the Pt_4Pd DTHs/C decreased by only 9.7% and 9.6%, respectively (Figure 4D). The TEM images showed that the morphology and size of the Pt_4Pd DTHs/C did not change much after 20 000 cycles (Supporting Information: Figure S16c). In contrast, Pt_2Pd DSHs/C showed 11% loss in SA and 10.9% loss in MA, along with 11.7 mV negative-shifted half-wave potential after 20 000 potential cycles (Supporting Information: Figure S11). After 20 000 cycles, Pt_3Pd DTHs/C showed a larger loss in SA (40.1%) and MA (39.4%), with a negative shift in the half-wave potential of 19.8 mV (Supporting Information: Figure S13). However, the commercial Pt/C showed a considerably larger negative shift (23.8 mV) in the ORR polarization curves, with 41.1% loss of SA, 41.6% loss of MA, and severe carbon corrosion (Supporting Information: Figure S10). The durability of Pd_4Pt DTHs/C, Pd_2Pt DSHs/C, Pd_3Pt DTHs/C, and commercial Pt/C toward the ORR was then evaluated through chronoamperometric (CA) measurements. The Pd_4Pt DTHs/C and Pd_2Pt DSHs/C showed minimal degradation of the current density (5.7% and 10.1%, respectively), whereas the Pd_3Pt DTHs/C and the commercial Pt/C catalysts maintained 73.4% and 66.2% of the current density, respectively (Supporting Information: Figure S17a). Compared with those of the as-prepared catalysts, the difference in the steady current density may be because the irreversible structural agglomeration of the Pd_3Pt DTHs/C and Pt/C catalysts resulted in a decrease in the active surface area of these catalysts and severe degradation of electrocatalyst durability, while the interaction between the Pt branch shell and the Pd nuclear substrate regulated the surface Pt electronic state, and Pt branches restrained dissolution and aggregation during long-term operation.[39] The slower current density decay manifested a much better stability of the Pd_4Pt DTHs/C and Pd_2Pt DSHs/C catalysts toward the ORR.

The Pd_4Pt DTHs/C, Pd_2Pt DSHs/C, Pd_3Pt DTHs/C, and commercial Pt/C were subjected to antipoisoning tests in the presence of 0.5 M CH_3OH. After the addition of CH_3OH to the O_2-saturated electrolyte at nearly 130 s, the Pd_4Pt DTHs/C showed a stable current response (only a decrease of 7.5%), whereas the current responses of the Pd_2Pt DSHs/C, Pd_3Pt DTHs/C, and commercial Pt/C decreased by 15.1%, 24.7%, and 26.4%, respectively (Supporting Information: Figure S17b). Pd_4Pt DTHs/C have strong resistance to methanol poisoning, mainly due to their unique structure and composition. First, the hollow structure of this catalyst can provide more active sites, thereby improving the catalytic efficiency and selectivity. Second, because of the composition of the Pt–Pd alloy, the catalyst exhibited excellent resistance to methanol poisoning. The synergistic effect of Pt and Pd can effectively prevent the catalyst surface from being covered by methanol molecules and maintain the activity of the catalyst surface. In addition, the dendritic structure also helps to increase the surface area of the catalyst, further enhancing its antipoisoning ability.[40] Overall, Pd_4Pt DTHs/C possess excellent antipoisoning ability and catalytic selectivity and much higher ORR activity than Pd_2Pt DSHs/C, Pd_3Pt DTHs/C and commercial Pt/C, making them the best Pt-based catalysts without any poisoning for fuel cell applications.

Compared with commercial Pt/C, we believe that the high catalytic activity and durability originates from its unique structure. (1) The hollow and porous tubular Pt–Pd bimetallic heterostructure can maximally expose Pt atoms on the inner and outer surfaces and provide plentiful active sites for high-efficient ORR catalytic reaction.[41–43] (2) The anisotropic 1D nanodendritic configuration could lead to multipoint contacts with the carbon support and reduce movement and aggregation, contributing to the excellent durability.[44–46] (3) The Pt nanobranches anchored on the Pd nanotube were interwoven and preferentially exposed (111) active facets, which could weaken Pt–O binding strength, leading to superior ORR activity.[47–49]

3 | CONCLUSION

In summary, we developed a general and robust approach for synthesis of a new class of 1D Pt–Pd dendritic nanotubular heterostructures by controlling the degree of Pt^{2+}-Pt reduction reaction and Pd-Pt galvanic replacement reaction with uniform Pd nanowires as sacrificial templates. The Pt–Pd dendritic nanotubular heterostructures exhibited considerably enhanced ORR activity compared to state-of-the-art commercial Pt/C catalysts. The as-prepared Pt_4Pd DTHs/C displayed an enhanced MA of 1.05 A mg_{Pt}^{-1} and SA of 1.25 mA cm_{Pt}^{-2} at 0.9 V versus RHE, nearly 4.8 and 4.3 times higher than that of the MA and SA of commercial Pt/C catalysts, respectively. Impressively, given its unique anisotropic 1D nanodendritic hollow configuration, the obtained Pt_4Pd DTHs/C are highly stable for ORR with negligible activity decay and structural degradation over the long-term course of 20 000 cycles. The Pt_4Pd DTHs/C catalyst also shows

excellent methanol tolerance surpassing that of the state-of-the-art Pt/C catalyst. We believe that this work will open up exciting opportunities toward the rational design of Pt–Pd bimetallic dendritic hollow nanostructures and will help guide the future development of electrocatalysts for their practical applications in renewable-energy-related devices and beyond.

4 | EXPERIMENTAL SECTION

4.1 | Chemicals and materials

Na_2PdCl_4 (98%), sodium iodide (NaI, 99.99%), isopropanol (AR, ≥99.5%), and Nafion (5 wt%) were purchased from Macklin. K_2PtCl_4 (98%) and perchloric acid ($HClO_4$, AR, 70.0% ~ 72.0%) were purchased from Aladdin. L-ascorbic acid ($C_6H_8O_6$, 99.99%), ethanol (C_2H_6O, AR, ≥99.7%), methanol (CH_4O, AR, 99.5%) and acetone (C_3H_6O, AR, ≥99.5%) were purchased from Shanghai Aladdin Chemical Reagent Company. Polyvinylpyrrolidone (PVP, Mw = 55 000) was purchased from Aldrich. Commercial Pt/C catalyst (20 wt%, 2–5 nm Pt nanoparticles) was purchased from Johnson Matthey (JM) Corporation. Deionized water (18.2 MΩ cm^{-1}) was used for all experimental processes, and all chemical reagents were used without further purification.

4.2 | Synthesis of Pd NWs

Na_2PdCl_4 (1.63 mg/mL), PVP (55.56 mg/mL), NaI (16.67 mg/mL), and 18 mL of deionized water were evenly mixed into a 25 mL Teflon-lined stainless-steel autoclave under vigorous stirring for 10 min. The sealed vessel was heated at 190°C for 2.5 h, and the Pd NWs suspensions were collected by centrifugation (10 000 rpm, 10 min) with ethanol/acetone/isopropanol (1:2:1) and further washed twice with ethanol/isopropanol (1:2). The product was obtained by centrifugation and washing for further use in the preparation of dendritic Pt–Pd bimetallic nanotubular heterostructure nanowires.

4.3 | Synthesis of Pt–Pd bimetallic NWs

For the Pt_4Pd DTHs, 2 mL of Pd NWs solution (10 mM), 1 mmol of PVP aqueous solution (1 ml), 0.25 mmol of L-ascorbic acid aqueous solution (5 mL) and 12 mL of ultrapure water were added to 50 mL of a two-necked flask and heated to 90°C under vigorous stirring. Meanwhile, 0.27 mmol K_2PtCl_4 aqueous solution (5 mL) was rapidly injected into the flask by a micropipette and heated at 90°C for 32 h under vigorous stirring. For the Pt_3Pd DTHs and Pt_2Pd DSHs, samples can be obtained by changing the content of L-ascorbic acid only to 0 mM and 60 mM. The prepared samples were collected by centrifugation (10 000 rpm, 10 min) with ethanol/isopropanol (1:2) and further washed twice with ethanol/isopropanol (2:1). The products were obtained by centrifugation and washing for further use in the characterization and electrochemical measurements.

4.4 | Characterization

X-ray diffraction (XRD) characterization was performed on a Bruker D8 X-ray diffractometer with Cu-$K\alpha$ radiation ($\lambda = 1.54056$ Å) operated at 40 kV and 40 mA. Transmission electron microscopy (TEM), high-resolution transmission electron microscopy (HRTEM), energy-dispersive X-ray spectroscopy, high-angle annular dark-field scanning transmission electron microscopy (HAADF-STEM), EDS mapping and line-scanning profiles were obtained using a Thermo Fisher Scientific Titan Themis G2 electron microscope fitted with aberration correctors for both probing lens and imaging lens at 300 kV. X-ray photoelectron spectroscopy (XPS) was recorded with a Thermo Scientific $K\alpha$ XPS spectrometer employing a monochromatic Al–$K\alpha$ X-ray source ($h\nu$ = 1486.6 eV). Inductively coupled plasma–optical emission spectrometry (ICP–OES) was used to determine the actual Pt loadings.

4.5 | Electrochemical measurements

All electrochemical measurements were performed on a CS310H electrochemical workstation with a three-electrode system with a rotating disk electrode (RDE) system. A graphite rod was used as the counter electrode, Ag/AgCl and Hg/HgO were used as the reference electrodes, and a glassy carbon electrode ($\varnothing = 5$ mm, $S = 0.196$ cm^{-2}) was used as the working electrode. The glassy carbon electrode was first polished by alumina powder with diameters of 1.5, 0.5, and 0.05 μm for 15 min and subsequently rinsed by sonicating in isopropyl and deionized water. Then, 0.98 mg of carbon-loaded catalyst was mixed in 20 μl of Nafion ionomer (5 wt%, Macklin) and 980 μl of ethanol solution (AR, ≥99.7%) to form the catalyst ink, and then 5 μL of the ink was dropped onto the surface of the glassy carbon electrode using a micropipette after sonication for 30 min in an ice bath. The catalyst ink was dried to deposit a high-quality catalyst thin film for electrochemical measurements with a rotation rate of 17 rpm for at least 15 min under

ambient conditions. The electrochemical tests for the Pt_3Pd DTHs, Pt_2Pd DSHs, Pt_4Pd DTHs, and Pt/C (20 wt%, JM) catalyst were measured under the same experimental conditions. The actual Pt loading for all the catalysts was kept at 6.5 $\mu g\,cm^{-2}$. All the loading masses were normalized over the geometric electrode area of 0.196 cm^{-2}.

Cyclic voltammograms (CVs) were obtained by scanning between 0.03 and 1.1 V versus RHE at a sweep rate of 50 $mV\,s^{-1}$ in N_2-saturated 0.1 M $HClO_4$ electrolyte solution. Linear scanning voltammetry (LSV) was performed from 0.2 to 1.1 V versus RHE at a sweep rate of 10 $mV\,s^{-1}$ in an O_2-saturated 0.1 M $HClO_4$ electrolyte solution with a rotation rate of 1600 rpm. The ORR accelerated durability tests (ADTs) were performed by cycling the potential between 0.2 and 1.1 V versus RHE in an O_2-saturated 0.1 M $HClO_4$ for potential cycles at a sweep rate of 50 $mV\,s^{-1}$ at room temperature.

The catalysts on the working electrodes were sonicated and dispersed in ethanol to observe the changes in morphology after the durability tests. The potential measured by the Ag/AgCl electrode could be transformed to the reversible hydrogen electrode (RHE) potential by the following equation:

$$E(\text{vs. RHE}) = E(\text{vs. Ag/AgCl}) + 0.197 + 0.059 \quad (1)$$

The specific ECSA was calculated based on the following equation:

$$\text{ECSA} = Q_H/m \times C, \quad (2)$$

where Q_H is the charge of H_{upd} adsorption, m is the Pt loading on the working electrode and C (210 $\mu C\,cm^{-2}$) is the charge obtained for monolayer adsorption of hydrogen on the Pt surface.

The specific kinetic current densities (j_k) can be obtained by the Koutecky–Levich equation:

$$1/j = 1/j_k + 1/j_d = 1/j_k + 1/B\omega^{1/2}, \quad (3)$$

where j is the experimentally measured current and j_d is the diffusion-limited current density. The parameter B was defined as follows:

$$B = 0.201nFC_oD_o^{2/3}\nu^{-1/6}, \quad (4)$$

where 0.201 for ω in units of rpm, n is the overall number of electrons, F is the Faraday constant (96 485 $C\,mol^{-1}$), C_o is the concentration of molecular oxygen in the electrolyte ($1.26 \times 10^{-6}\,mol\,cm^{-3}$), D_o is the diffusion coefficient of the molecular O_2 in 0.1 M $HClO_4$ solution ($1.93 \times 10^{-5}\,cm^2\,s^{-1}$), and ν is the viscosity of the electrolyte ($1.009 \times 10^{-2}\,cm^2\,s^{-1}$).

The stability of the catalysts was investigated by chronoamperometry in O_2-saturated 0.1 M KOH electrolyte solution for 10 h by applying a potential of 0.6 V. To test methanol effects on ORR activity, the as-synthesized catalysts determined by the addition of methanol during the chronoamperometry test at 1600 rpm and a scan rate of 10 $mV\,s^{-1}$ in O_2-saturated 1 M KOH.

ACKNOWLEDGMENTS

This work is financially supported by National Natural Science Foundation of China (52072281) and the Major Program of the National Natural Science Foundation of China (22293021). Y. L. gratefully acknowledges Youth Innovation Research Fund project of State Key Laboratory of Advanced Technology for Materials Synthesis and Processing, Wuhan University of Technology.

CONFLICT OF INTEREST STATEMENT

The authors declare no conflict of interests.

ORCID

Baolian Su http://orcid.org/0000-0001-8474-0652
Yong Liu http://orcid.org/0000-0002-1469-0757

REFERENCES

[1] Yang C-L, Wang L-N, Yin P, et al. Sulfur-anchoring synthesis of platinum intermetallic nanoparticle catalysts for fuel cells. *Science*. 2021;374:459-464.
[2] Wang XX, Swihart MT, Wu G. Achievements, challenges and perspectives on cathode catalysts in proton exchange membrane fuel cells for transportation. *Nat Catal*. 2019;2:578-589.
[3] Sun Y, Polani S, Luo F, Ott S, Strasser P, Dionigi F. Advancements in cathode catalyst and cathode layer design for proton exchange membrane fuel cells. *Nat Commun*. 2021;12:5984.
[4] Seh ZW, Kibsgaard J, Dickens CF, Chorkendorff I, Nørskov JK, Jaramillo TF. Combining theory and experiment in electrocatalysis: insights into materials design. *Science*. 2017;355(65321):eaad4998.
[5] Peng Y, Choi J-Y, Fürstenhaupt T, Bai K, Zhang Y, Banham D. New approach for rapidly determining Pt accessibility of Pt/C fuel cell catalysts. *J Mater Chem A*. 2021; 9:13471-13476.
[6] Lou Y, Li C, Gao X, et al. Porous pt nanotubes with high methanol oxidation electrocatalytic activity based on original bamboo-shaped te nanotubes. *ACS Appl Mater Interfaces*. 2016;8:16147-16153.
[7] Bu L, Guo S, Zhang X, et al. Surface engineering of hierarchical platinum-cobalt nanowires for efficient electrocatalysis. *Nat Commun*. 2016;7:11850.
[8] Wang W, Lv F, Lei B, Wan S, Luo M, Guo S. Tuning nanowires and nanotubes for efficient fuel-cell electrocatalysis. *Adv Mater*. 2016;28:10117-10141.
[9] Liu M, Xu Y, Liu S, et al. Phosphorus-modified ruthenium-tellurium dendritic nanotubes outperform platinum for

alkaline hydrogen evolution. *J Mater Chem A*. 2021;9:5026-5032.

[10] Hao Y, Yang Y, Hong L, Yuan J, Niu L, Gui Y. Facile preparation of ultralong dendritic PtIrTe nanotubes and their high electrocatalytic activity on methanol oxidation. *ACS Appl Mater Interfaces*. 2014;6:21986-21994.

[11] Zhang H, Jin M, Liu H, et al. Facile synthesis of Pd–Pt alloy nanocages and their enhanced performance for preferential oxidation of CO in excess hydrogen. *ACS Nano*. 2011;5:8212-8222.

[12] Hong JW, Kang SW, Choi B-S, Kim D, Lee SB, Han SW. Controlled synthesis of Pd–Pt alloy hollow nanostructures with enhanced catalytic activities for oxygen reduction. *ACS Nano*. 2012;6:2410-2419.

[13] Huang X, Zheng N. One-pot, high-yield synthesis of 5-fold twinned Pd nanowires and nanorods. *J Am Chem Soc*. 2009;131:4602-4603.

[14] Wang G-H, Chen K, Engelhardt J, et al. Scalable one-pot synthesis of yolk-shell carbon nanospheres with yolk-supported Pd nanoparticles for size-selective catalysis. *Chem Mater*. 2018;30:2483-2487.

[15] Gao Z, Ye H, Wang Q, et al. Template regeneration in galvanic replacement: a route to highly diverse hollow nanostructures. *ACS Nano*. 2020;14:791-801.

[16] Ghosh S, Mondal S, Retna Raj C. Carbon nanotube-supported dendritic Pt-on-Pd nanostructures: growth mechanism and electrocatalytic activity towards oxygen reduction reaction. *J Mater Chem A*. 2014;2:2233-2239.

[17] Chen Y, Niu H-J, Feng Y-G, et al. Three-dimensional hierarchical urchin-like PdCuPt nanoassembles with zigzag branches: a highly efficient and durable electrocatalyst for formic acid oxidation reaction. *Appl Surf Sci*. 2020;510:145480.

[18] Crockett JR, Wang M, Doebler JE, Pawale T, Li X, Bao Y. Impact on the formation and catalytic property of Pt-based nanocatalysts by galvanic reaction with Co-reduction agents. *Chem Mater*. 2022;34:9282-9293.

[19] Wang L, Nemoto Y, Yamauchi Y. Direct synthesis of spatially-controlled Pt-on-Pd bimetallic nanodendrites with superior electrocatalytic activity. *J Am Chem Soc*. 2011;133:9674-9677.

[20] Zhao F, Zheng L, Yuan Q, et al. Ultrathin PdAuBiTe nanosheets as high-performance oxygen reduction catalysts for a direct methanol fuel cell device. *Adv Mater*. 2021;33:2103383.

[21] Xu Y, Wu D, Deng P, et al. Au decorated Pd nanowires for methane oxidation to liquid C1 products. *Appl Catal B*. 2022;308:121223.

[22] Jin H, Wei X, Zhao L, et al. Modulating the alloying mode in the doping-induced synthesis of Au-Pd nanowires. *Nano Res*. 2023;15:2488-2515.

[23] Yang L, Li G, Chang J, et al. Sea urchin-like $Au_{core}@Pd_{shell}$ electrocatalysts with high FAOR performance: coefficient of lattice strain and electrochemical surface area. *Appl Catal B*. 2020;260:118200.

[24] Zhang R-L, Duan J-J, Mei L-P, Feng JJ, Yuan PX, Wang AJ. Facile synthesis of porous iridium-palladium-plumbum wire-like nanonetworks with boosted catalytic performance for hydrogen evolution reaction. *J Colloid Interface Sci*. 2020;580:99-107.

[25] Liu R, Zhao H, Zhao X, et al. Defect sites in ultrathin pd nanowires facilitate the highly efficient electrochemical hydrodechlorination of pollutants by H^*_{ads}. *Environ Sci Technol*. 2018;52:9992-10002.

[26] Li X, Han X, Yang Z, et al. Lattice-distorted Pt wrinkled nanoparticles for highly effective hydrogen electrocatalysis. *Nano Res*. 2024;17:3819-3826.

[27] Hu Y, Zhu M, Luo X, et al. Coplanar Pt/C nanomeshes with ultrastable oxygen reduction performance in fuel cells. *Angew Chem Int Ed*. 2021;60:6533-6538.

[28] Denisov N, Qin S, Will J, et al. Light-induced agglomeration of single-atom platinum in photocatalysis. *Adv Mater*. 2023;35:e2206569.

[29] Zhang Y, Zhao L, Walton J, Liu Z, Tang Z. Facile fabrication of PtPd alloyed worm-like nanoparticles for electrocatalytic reduction of oxygen. *Int J Hydrogen Energy*. 2017;42:17112-17121.

[30] Lopes T, Antolini E, Gonzalez E. Carbon supported Pt–Pd alloy as an ethanol tolerant oxygen reduction electrocatalyst for direct ethanol fuel cells. *Int J Hydrogen Energy*. 2008;33:5563-5570.

[31] Liu C-H, Porter S, Chen J, et al. Enhanced low temperature performance of bimetallic $Pd/Pt/SiO_2$(core) @Zr(shell) diesel oxidation catalysts. *Appl Catal B*. 2023;327:122436.

[32] Ando F, Gunji T, Tanabe T, et al. Enhancement of the oxygen reduction reaction activity of Pt by tuning its d-band center via transition metal oxide support interactions. *ACS Catal*. 2021;11:9317-9332.

[33] Wang W, Wang Z, Wang J, Zhong CJ, Liu CJ. Highly active and stable Pt–Pd alloy catalysts synthesized by room-temperature electron reduction for oxygen reduction reaction. *Adv Sci*. 2017;4:1600486.

[34] Liu W, Rodriguez P, Borchardt L, et al. Bimetallic aerogels: high-performance electrocatalysts for the oxygen reduction reaction. *Angew Chem Int Ed*. 2013;52:9849-9852.

[35] Park J, Wang H, Vara M, Xia Y, et al Platinum cubic nanoframes with enhanced catalytic activity and durability toward oxygen reduction. *ChemSusChem*. 2016;9:2855-2861.

[36] Zhang H, Jin M, Wang J, et al. Synthesis of Pd–Pt bimetallic nanocrystals with a concave structure through a bromide-induced galvanic replacement reaction. *J Am Chem Soc*. 2011;133:6078-6089.

[37] Jebaslinhepzybai BT, Prabu N, Sasidharan M. Facile galvanic replacement method for porous Pd@Pt nanoparticles as an efficient HER electrocatalyst. *Int J Hydrogen Energy*. 2020;45:11127-11137.

[38] Cho EC, Camargo PHC, Xia Y. Synthesis and characterization of noble-metal nanostructures containing gold nanorods in the center. *Adv Mater*. 2010;22:744-748.

[39] Maghsodi A, Milani Hoseini MR, Dehghani Mobarakeh M, et al. Exploration of bimetallic Pt–Pd/C nanoparticles as an electrocatalyst for oxygen reduction reaction. *Appl Surf Sci*. 2011;257:6353-6357.

[40] Feng Y, Shao Q, Lv F, et al. Intermetallic PtBi nanoplates boost oxygen reduction catalysis with superior tolerance over chemical fuels. *Adv Sci*. 2020;7:1800178.

[41] Tao L, Yu D, Zhou J, Lu X, Yang Y, Gao F. Ultrathin wall (1 nm) and superlong Pt nanotubes with enhanced oxygen reduction reaction performance. *Small*. 2018;14:e1704503.

[42] Lim B, Jiang M, Camargo PHC, et al. Pd–Pt bimetallic nanodendrites with high activity for oxygen reduction. *Science*. 2009;324:1302-1305.
[43] Jin H, Xu Z, Hu Z-Y, et al. Mesoporous Pt@Pt-skin Pt_3Ni core-shell framework nanowire electrocatalyst for efficient oxygen reduction. *Nat Commun*. 2023;14:1518.
[44] Xu F, Cai S, Lin B, Yang L, Le H, Mu S. Geometric engineering of porous PtCu nanotubes with ultrahigh methanol oxidation and oxygen reduction capability. *Small*. 2022;18:2107387.
[45] Nie Y, Sun Y, Song B, et al. Low-electronegativity Mn-contraction of PtMn nanodendrites boosts oxygen reduction durability. *Angew Chem Int Ed*. 2024;63:e202317987.
[46] An Z, Li H, Zhang X, et al. Structural evolution of a PtRh nanodendrite electrocatalyst and its ultrahigh durability toward oxygen reduction reaction. *ACS Catal*. 2022;12:3302-3308.
[47] Zhang J, Yuan Y, Gao L, Zeng G, Li M, Huang H. Stabilizing Pt-based electrocatalysts for oxygen reduction reaction: fundamental understanding and design strategies. *Adv Mater*. 2021;33:2006494.
[48] Xu H, Shang H, Wang C, Du Y. Ultrafine Pt-based nanowires for advanced catalysis. *Adv Funct Mater*. 2020;30:2000793.
[49] Liu Z, Zhao Z, Peng B, Duan X, Huang Y. Beyond extended surfaces: understanding the oxygen reduction reaction on nanocatalysts. *J Am Chem Soc*. 2020;142:17812-17827.

SUPPORTING INFORMATION

Additional supporting information can be found online in the Supporting Information section at the end of this article.

How to cite this article: Wang M, Hu Z, Lv J, et al. Construction of dendritic Pt–Pd bimetallic nanotubular heterostructure for advanced oxygen reduction. *Interdiscip Mater*. 2024;3:907-918. doi:10.1002/idm2.12212